Stretchable wideband dipole antennas and rectennas for RF energy harvesting

Jia Zhu [a], Zhihui Hu [a, b], Chaoyun Song [c], Ning Yi [d], Zhaozheng Yu [a], Zhendong Liu [a, e], Shangbin Liu [a, f], Mengjun Wang [g], Michael Gregory Dexheimer [a], Jian Yang [h], Huanyu Cheng [a, d, f, h, *]

[a] Department of Engineering Science and Mechanics, USA
[b] School of Logistics Engineering, Wuhan University of Technology, Wuhan, 430063, China
[c] School of Engineering and Physical Sciences, Heriot-Watt University, Edinburgh, EH14 4AS, Scotland, UK
[d] Department of Materials Science and Engineering, USA
[e] Key Laboratory of E&M, Zhejiang University of Technology, Ministry of Education & Zhejiang Province, Hangzhou, Zhejiang, 310014, China
[f] Department of Mechanical Engineering, USA
[g] School of Electronics and Information Engineering, Hebei University of Technology, Tianjin, 300401, China
[h] Department of Biomedical Engineering, The Pennsylvania State University, University Park, PA, 16802, USA

ARTICLE INFO

ABSTRACT

The ultimate application of bio-integrated, stretchable electronics hinges on the indispensable modules of stretchable wireless data transmission and power supplies. While radiofrequency (RF) antennas and rectennas could enable wireless communication and RF energy harvesting in the far-field, their performance deteriorates because of the frequency detuning from mechanical deformations. Here, stretchable wideband antennas and rectennas are introduced to robustly operate and combine received RF power over their wideband upon mechanical deformations. Devices with stretchable wideband antennas and rectennas create application opportunities such as self-powered systems, remote monitoring of the environment, and clean energy. A comprehensive set of manufacturing schemes, device components, and theoretical design tools for the stretchable wideband antennas and rectennas is reported. A stretchable wideband rectenna integrated with various functional sensing modules and its demonstration with enhanced effective efficiency over the state-of-the-art by 10−100 times illustrates a system-level example of this technology.

1. Introduction

Capable of pliably conforming to the textured skin surface to continuously monitor the physiologically relevant parameters or biomarkers, bio-integrated electronics have a significant impact on human health from preventative monitoring and early diagnostic confirmation to non-invasive and convenient therapeutic options [1−3]. The ultimate application of this class of emerging electronics hinges on the indispensable modules of stretchable wireless data transmission and power supplies [3]. Based on simple inductive coupling, the near field communication (NFC) provides wireless powering and communication of various sensors [4,5] that measure physiological parameters, including pressure [6], temperature [7], and pulse oxygen level [8]. However, the limited working distance (~3 cm) [9,10] implies a close placement of receiving devices and external sources, presenting the challenge in continuous monitoring. While the use of a coil array or coils with a larger size can increase the working distance, they inevitably increase the system footprint and integration complexity [11]. As an alternative, radiofrequency (RF) antennas enable wireless transmission of data and energy in the far-field (e.g., in the range of meters) [12,13].

While stretchable conducting materials [14−16] such as liquid metal in soft microfluidic channels or elastomers with conductive fillers have been explored for stretchable antennas, designing conventional metals in a serpentine or meshed geometry [17,18] is still of great interest because of their high radiation efficiency. Although this structural design concept has resulted in various stretchable dipole and patch antennas [17,19], the small bandwidth

* Corresponding author. Department of Engineering Science and Mechanics, USA.
E-mail address: Huanyu.Cheng@psu.edu (H. Cheng).

still limits their applications in wireless communication and energy harvesting because of the frequency detuning from mechanical deformations. While the efforts on wideband antennas (e.g., engraving slots on the bowtie dipole antennas [20] or including parasitic arms to couple multiple resonances [21–23]) could overcome this challenge, the deformation-dependent radiation properties are yet to be thoroughly investigated.

Connecting the antenna with a rectifying circuit results in a rectifying antenna (rectenna). Ambient RF energy harvesting through a rectenna can continuously generate direct current (DC) power [20,24] to power sensors or charge energy storage devices, providing an always-on solution for wearable electronics [25–27] and remote sensors [28]. However, the performance of rectennas significantly deteriorates because of the frequency detuning from mechanical deformations such as bending or stretching. While the miniaturized, thin-film design of the rectifying circuit and matching network could provide a robust mechanical property, the size of the antenna in the rectenna is limited to a specific range for the target frequency band(s) of ambient wireless energies [29]. Additionally, the conversion efficiency of state-of-the-art rectennas from any single frequency is significantly reduced at low ambient RF powers (« 1 mW) [25,30,31]. It is partially because of the limiting diode characteristics and a high loss in the antenna and impedance matching circuits [31]. Therefore, it is of critical importance to design and demonstrate stretchable wideband rectennas with a high-performance, stretchable wideband antenna to combine received RF energy over their broadband upon deformations.

Here, we present a stretchable wideband antenna and rectenna for wireless transmission and ambient RF energy harvesting. Following the coupled mechanics-electromagnetic design, stretchable wideband dipole antennas consisting of serpentine units have been experimentally demonstrated with deformation-independent radiation properties. Next, connecting the stretchable wideband dipole antenna with a rectifying circuit yields a high-efficiency stretchable rectenna to continuously harvest the ambient RF energy from various widely available RF sources (e.g., Wi-Fi, 4G, microwave oven, and possibly upcoming 5G). The direct current (DC) power continuously generated from ambient RF energy harvesting can be used by external loads or to charge energy storage devices (e.g., batteries and supercapacitors). The ambient RF energy harvesting could also be exploited for implantable electronics [32] to monitor real-time physiological conditions and deliver drugs [33] or medical treatment [34], promising the possible integration with the recent development of transient electronics [35]. Integrating the wireless transmission and energy harvesting modules with various laser-fabricated sensors could enable self-powered wearable electronics to open up a new frontier for diagnostic monitoring and therapeutic options.

1.1. Laser-fabricated stretchable wideband antennas/rectennas with other sensing modules

As an illustrative example, we present stretchable wideband dipole antennas for wireless communication and ambient RF energy harvesting (Fig. 1A) because of their simple design and omnidirectional radiation properties. Because of their high radiation efficiency and electromagnetic properties, conventional metals with stretchable structures (e.g., a serpentine or meshed geometry [17,18]) can be explored for the radiation elements. Fabrication of stretchable metal antennas combines conductive laser-induced graphene (LIG) patterns (Fig. S1) [36] with a selective metal surface coating (Figure S2 to S4) on an elastomeric substrate (Figure S5). With the Ag surface coating, the sheet resistance is reduced from 28.5 ± 1.5 Ω/□ in the LIG to 1.2 ± 0.06 Ω/□ in the Ag/LIG, enabling its applications in RF devices. Integrating the wireless

transmission and energy harvesting modules with various LIG sensors [37] could also enable the flexible/stretchable all-LIG electronics to open up a new frontier for diagnostic monitoring and therapeutic options. Fast laser fabrication (<30 min) yields a representative all-LIG electronic device on the polyimide (PI) film (Fig. 1C). The potential all-LIG device consists of conductive traces and contact pads, various sensing modules, and complementary communication and powering modules (i.e., NFC coil for near-field [38] and dipole antenna for far-field), illustrating the possibility to go from individual components to the integrated system. Transferring the device onto a stretchable Ecoflex substrate completes the fabrication of a stretchable all-LIG device (Fig. 1D). Besides the demonstrated sensing and wireless modules, the commercial off-the-shelf (COTS) chips such as a microcontroller can be soldered through the metal-coated pins.

In this proof-of-concept demonstration, each individual component has been separately investigated. The LIG temperature sensor patterned in a serpentine trace demonstrates good sensitivity and linearity in the temperature range from 0 to 100 °C (Fig. 1E). A humid sensor designed in the Archimedean spiral shows a frequency-dependent increase in the measured capacitance as the relative humidity increases (Fig. 1F). The winding and spiral structures of the temperature and humid sensors can ensure their stable and reliable sensing performance under mechanical deformations (Figure S6AB). For example, the resistance-based temperature sensor shows a negligible change upon stretching (e.g., <1% for a 20% stretching), implying stable and reliable temperature sensing performance even under deformations. Similar to previously reported results [37,39], 20% stretching applied to the humidity sensor only leads to a ~1.2% change in capacitance, implying reliable humidity measurement upon deformations. The two small LIG electrodes with a size of 3 mm × 3 mm are also able to capture high-fidelity electrophysiological (EP) signals such as an electrocardiogram (ECG) (Fig. 1G). The use of serpentine and meshed structures (Figure S6C) can also provide stretchable electrodes for measurements of other EP signals, as in the previous studies [38]. Details of the measurement process can be found in the Method section. The dipole antenna has been connected to a rectifying circuit (see Figure S7 for the design) [20], and the harvested energy can be used to power the sensing modules through connection to the microcontroller. A power management circuit (PMC) is also needed to stabilize and regulate the DC output voltage from the rectenna. As an example, the TI BQ25504 chipset is used as the PMC to result in the completed system, with the block diagram provided in Figure S8. Despite the demonstrated sensing modules, this work still focuses on the design, fabrication, and demonstration of the stretchable antenna/rectenna.

1.2. Stretchable wideband dipole antennas from the dual-resonance

Because of the PI self-mask formed by the laser cutting process, the Ag nanoparticles ink can be precisely dispersed on the patterned LIG/PI composite, followed by photonic sintering to result in a conductive Ag layer. The PI underneath the Ag/LIG layer serves as a stiffener to help reduce the local strain in the conductive pattern upon deformations. The design of the stretchable wideband antennas relies on the use of the software ABAQUS for finite element analysis (FEA) and ANSYS HFSS for antenna simulations. In contrast to the dipole antennas with the straight arms, wavy serpentine structures are first adopted in the radiation arms to render stretchable dipole antennas. To overcome the challenge of frequency detuning in the dipole antennas with a narrow bandwidth, the parasitic arms are introduced next to the driven arms to provide a capacitive load for enabling wideband capabilities. The wideband capabilities result from the coupling between two
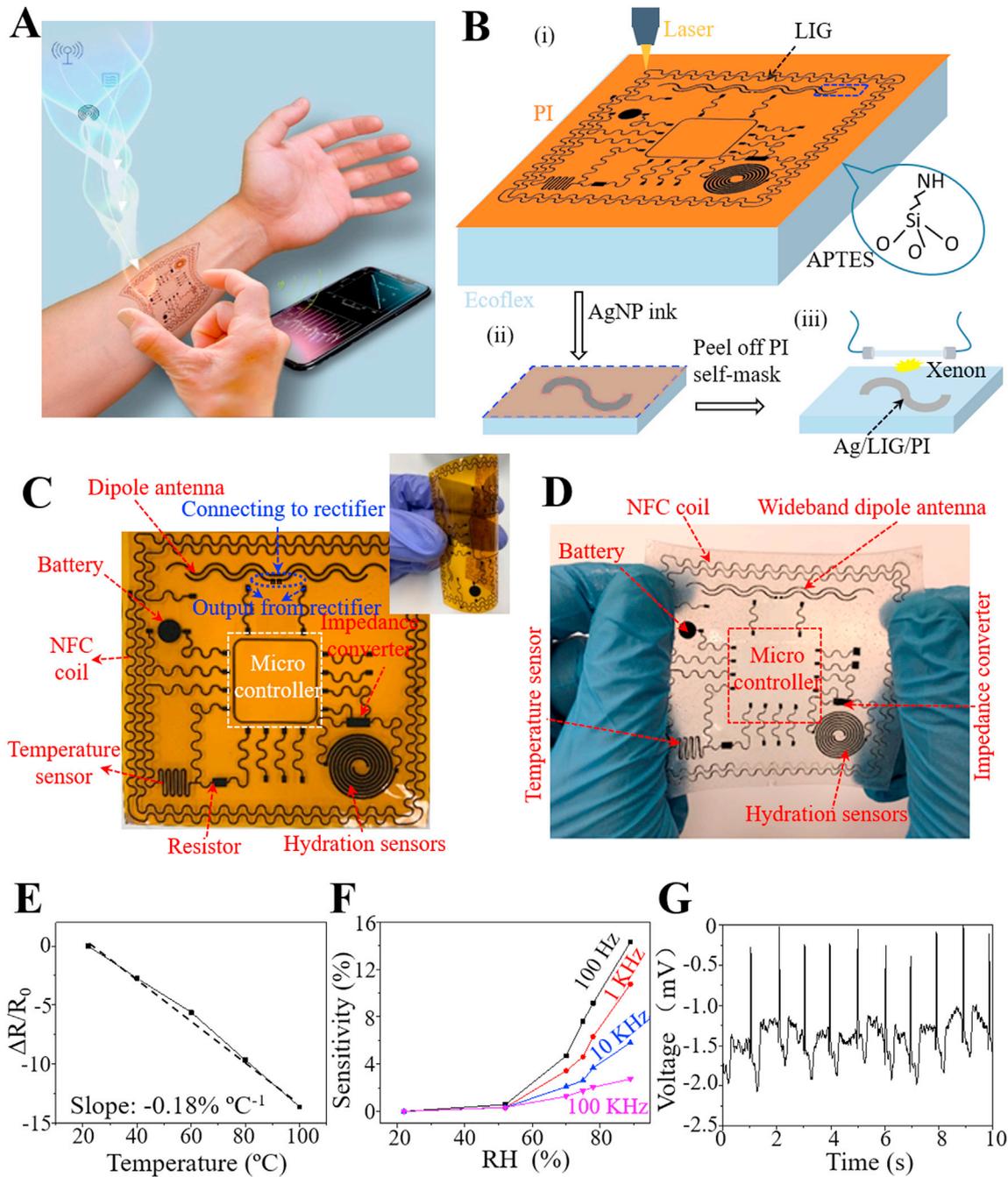
Fig. 1. Demonstration platform of stretchable wideband antennas and rectennas for wireless communication and ambient RF energy harvesting and their use in all laser fabricated devices. (A) Illustration of the laser fabricated device on the skin upon deformation with various sensing modules and a stretchable wideband antenna/rectenna for wireless communication and ambient RF energy harvesting. **(B)** Schematic illustration of the fabrication process to prepare laser-induced graphene (LIG) patterns on polyimide (PI) and a subsequent metal surface coating for LIG sensors and the stretchable wideband antenna/rectenna. Depending on the desired spatial resolution for the pattern, the CO_2, UV, or femtosecond laser can be explored. The electro(less) plating can also be explored for the selective surface coating. APTES: (3-Aminopropyl)triethoxysilane. **(C)** The Optical image shows a flexible all-LIG electronic device that includes near-field communication (NFC) coil for short-range communication, wideband dipole antenna for RF long-range communication, sensing units (i.e., temperature sensor, hydration sensor, and electrodes for electrophysiological signal monitoring), pins to connect commercially off-the-shelf (COTS) chips (COTS chips and metal surface coating not shown for clarity). The antenna connected to an external rectifying circuit (not shown) can be used to harvest the ambient RF energy with output connected to the microcontroller for powering. **(D)** Laminating the device in **(C)** on Ecoflex substrates and removing the PI mask yield the stretchable all-LIG electronics. **(E)** Measured resistive response of the LIG temperature sensor under stretching. The linear fitting of the measured curve gives a slope of -0.18% °C^{-1}. **(F)** Measured capacitive response of the LIG hydration sensor with an Archimedean spiral configuration in different relative humidity (RH) levels at three frequencies. **(G)** Electro-cardiogram (ECG) signal measured by two LIG electrodes with a size of 3 mm × 3 mm.

resonant states, with one from the driven arms and the other from the parasitic arms. The simulation software ANSYS HFSS has been further used to investigate the effect of various design parameters for revealing the coupling mechanism and guiding the antenna design.

The stretchable wideband dipole antenna is designed to couple two resonance states from both parasitic and driven arms, both of which are shaped into serpentine layouts with circular arc unit

elements and a width w of 0.4 mm (Figure S9). Each unit element has two arcs with the same arc angle but different radii. Changing radiation elements from straight to serpentine shapes of the same actual length slightly reduces the resonant frequency of dipole antennas. For example, compared to the dipole antenna with straight arms, the stretchable dipole antenna with serpentine arms of the same apparent length ($L_{app.}$ = 47.2 mm, see Figure S9 for definitions) resonates at a lower frequency because of its longer actual length ($L_{act.}$ = 56.2 mm). However, this serpentine dipole antenna still has a higher resonant frequency than that of the straight dipole antenna with the same actual length of $L_{act.}$, likely attributed to the geometric effect (Figure S10). In contrast to the dipole antennas without parasitic arms (Figure S11) or with unconnected parasitic arms (Figure S12), the dipole antennas with connected parasitic arms exhibit a strong coupling effect with two resonances ("double-peak") in the S_{11} curve (Fig. 2AB). It is confirmed by the simulated electric field and surface current distribution that the two resonances originate from the two pairs of radiation arms (Fig. 2C). The stronger coupling effect in the antenna with connected parasitic arms leads to a much larger bandwidth (Fig. 2D) than the other two antennas (Figure S13, Table S1 and S2). Within the bandwidth, the wideband antenna with connected parasitic arms could transmit 90% of the input power with a standing wave ratio of ~2.

Because the bandwidth relies on the coupling of two resonance states, changing the relative lengths between driven and parasitic arms represents an easy method to tune the bandwidth. However, the bandwidth does not monotonically increase with the relative length difference between driven and parasitic arms (Fig. 2A). With the apparent length of the long parasitic arm fixed to an apparent length of 56.2 mm, the antenna with the shortest driven arms (apparent length of 37.0 mm) shows the largest difference between the two resonances. However, a significantly increased reflection loss due to the degraded impedance matching to 50 Ω ports from the parasitic effect severely degenerates its wideband property. Because of the split of two resonance states, strong coupling effect (Figure S14), and excellent impedance matching (Figure S15), the stretchable wideband antenna with a proper relative length difference exhibits the largest bandwidth (i.e., the apparent length of 39.2 mm in driven arms). This configuration is denoted as the stretchable wideband antenna in the following discussion unless otherwise specified. Of note, the pair of short arms is chosen as the driven arms (i.e., feed location) due to better impedance match to the 50 Ω port, which is opposite to the straight dipole antennas with parasitic arms. The coupling strength also depends on the gap between driven and parasitic arms. The decrease in the gap results in an increased bandwidth (Figure S16 and S17). Different from dipole antennas with straight arms, simply bringing the driven arms closer to the parasitic arms yields a non-uniform spacing between the two. A uniform decrease in the spacing can be designed by reducing the radius of outer arcs and the length in the driven arms. For instance, uniformly reducing the space from 0.8 to 0.6 mm leads to a slight shift in the frequency to the higher value in the S_{11} (Fig. 2B). Other than the shift in the frequency, the bandwidth only decreases slightly from 0.45 GHz to 0.42 GHz by 6.7%. The negligible change in the bandwidth implies the possibility to further reduce the footprint of stretchable dipole antennas. The change in the conductivity of radiation elements could also tune the coupling, but a proper value ensures optimized values in both bandwidth and efficiency (Figure S18).
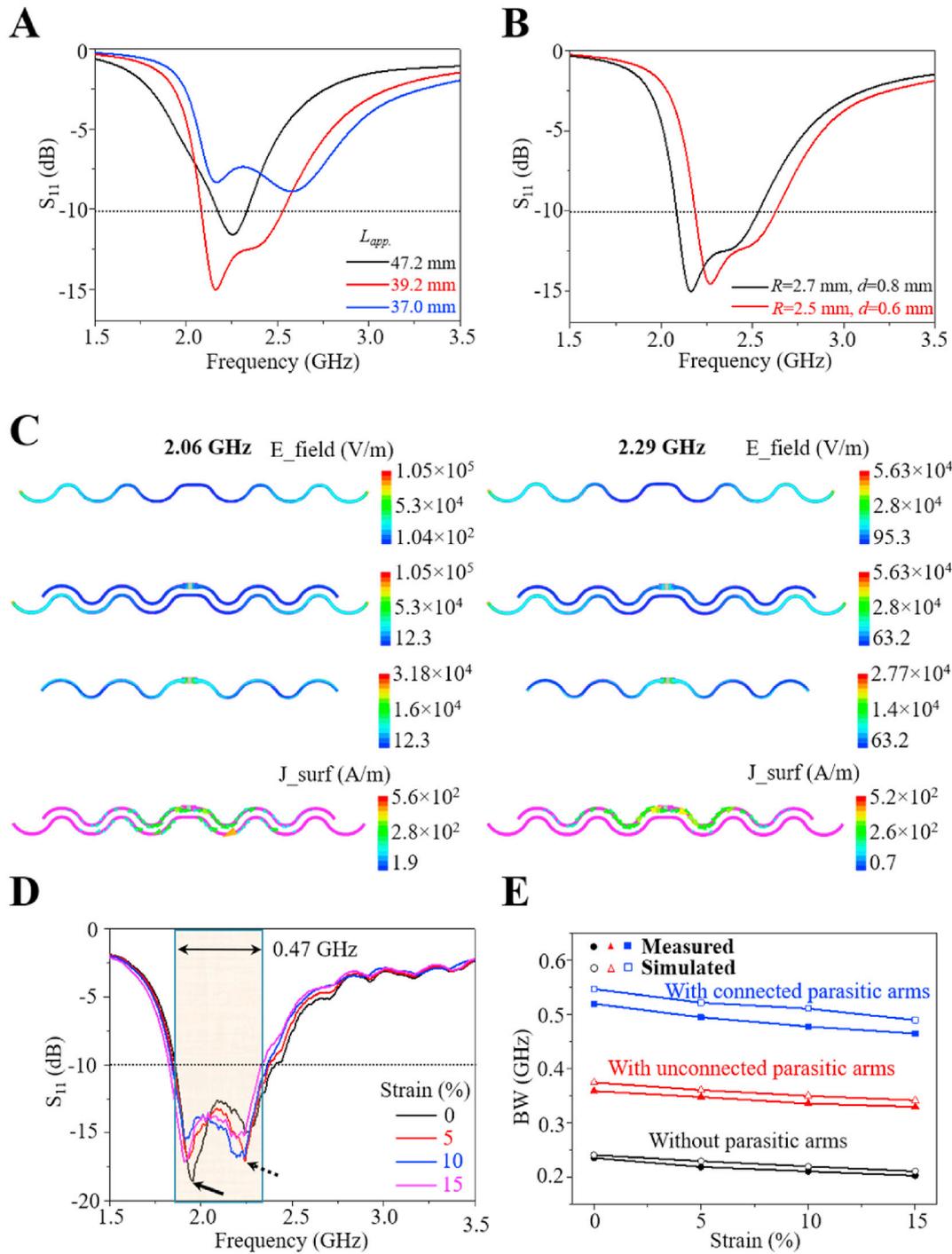
1.3. Coupled mechanical-electromagnetic properties of stretchable wideband dipole antennas

The coupled mechanical-electromagnetic properties of the stretchable dipole antenna are revealed by evaluating its radiation performance upon the tensile strain with a customized stretcher (Figure S19). To avoid the localized high strain at the feed location upon stretching, the encapsulation with location-dependent stiffness [14] can be explored. By exploiting a stiff PDMS encapsulant for the soldered feed location and a soft Ecoflex encapsulant for the rest (Figure S20), the strain at the feed location is vanishing upon a tensile strain of 15%, confirming the effectiveness of this strain-isolation design (Movies S1 and **S2**). While the strain in Ecoflex reaches ~100%, the maximal strain in the radiation patterns is ~3% due to the unfolding of serpentine arms [17,40] and strain isolation effect [41,42] from the stiff PI layer underneath the Ag/LIG pattern. Although considering the out-of-plane buckling of the arms has a minor influence on simulated S_{11} curves, it further reduces the peak strain (Figure S21). Upon stretching, the serpentine arms unfold to increase the apparent length of the antenna along the direction of the tensile strain, leading to a decrease in frequency for all the stretchable antennas with serpentine radiation arms (Fig. 2D). Interestingly, the frequency shift of ~0.01 GHz in the stretchable wideband antenna is negligibly small. The "double-peak" characteristic in S_{11} curves is also not affected by the stretching. The bandwidth decreases by 0.02 GHz as the applied tensile strain increases to 15% (Fig. 2E). Compared with the antenna without (Figure S13A) or with unconnected parasitic arms (Figure S13B), the stretchable wideband antenna has larger bandwidth under all tensile strain levels. After defining the operating bandwidth of the stretchable antennas as the overlapping bandwidth over the range of the applied tensile strain (shaded areas in Fig. 2D), the operating bandwidth is observed to decrease with the increasing tensile strain due to the shift of S_{11} curves and a relative constant bandwidth. Owing to the small changes in the frequency shift and large bandwidth upon stretching, the operating bandwidth of the stretchable wideband antenna demonstrates a significant increase in the operating bandwidth of 0.47 GHz over the antenna without (0.14 GHz) or with unconnected (0.23 GHz) parasitic arms (Figure S13). Additionally, the radiation patterns of the stretchable dipole antennas with and without parasitic arms at resonance illustrate negligible changes, highlighting stable performance upon tensile deformations (Figure S23).

Supplementary data related to this article can be found at https://doi.org/10.1016/j.mtphys.2021.100377.

Besides stretching, the stretchable wideband dipole antenna also exhibits robust performance against the other deformation modes such as bending and twisting (Fig. 3A and S24). The "double-peak" characteristic in S_{11} curves for the stretchable wideband dipole antenna is well maintained even with large bending and twisting deformations, with a radius of curvature of 40 mm in the former and a twisting angle of 360° in the latter. Furthermore, the FEA simulation results indicate small local strain values in the conductive patterns of the antenna upon bending and twisting deformations (Fig. 3B), which supports the mechanically robust and durable radiation properties of the antenna. Compared to stretching, bending and twisting result in little changes in the lengths of or spacing between driven and parasitic arms. The nearly unaffected coupling between driven and parasitic arms upon bending deformations led to a negligibly small change in the S_{11} curve (Fig. 3C). Besides S_{11} curves, the main characteristics in impedance curves (i.e., the peak and inflection points in the real and imaginary parts) and radiation patterns (Figure S25) also only exhibit negligible changes upon bending deformations, as indicated in the simulated results (Figure S26). The durable antenna performance has also been confirmed after cyclic stretching and bending deformations of 1000 times (Figure S27). No obvious change in the morphology of the Ag/LIG radiation arm is observed after the fatigue testing, which is attributed to the serpentine design, location-
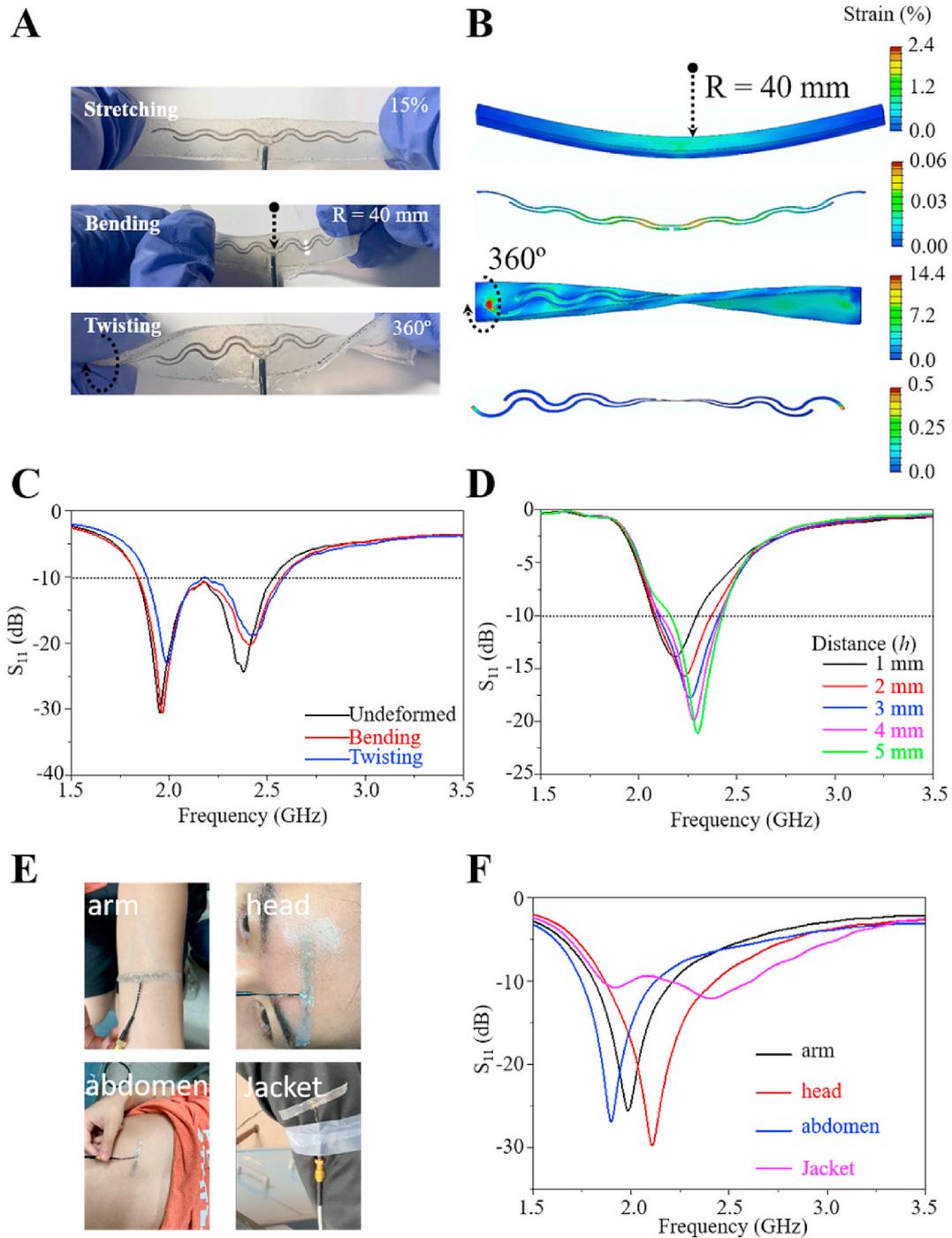
Fig. 2. Design of the stretchable wideband antenna and its mechanical-electromagnetic properties. (A) Influence of the relative length difference between driven and parasitic arms on the S_{11} curve of the antenna. The apparent length of driven arms ($L_{app.}$) varies (i.e., 37.0, 39.2, and 45.1 mm), whereas the parasitic arms are fixed at a length of 47.2 mm. Bandwidth is defined as the frequency range with S_{11} values lower than −10 dB (corresponding to a standing wave ratio of ~2), as indicated by the dotted lines. **(B)** Influence of the uniform gap between the driven and parasitic arms as it reduces from 0.8 to 0.6 mm (while fixing the inner radius at 1.2 mm and changing the outer radius from 2.7 to 2.5 mm). **(C)** Simulated electric field (E_field) and surface current (J_surf) distribution of the "FS-Connected-I" (stretchable wideband) antenna at resonance at two resonance frequencies 2.06 and 2.29 GHz, respectively. The size of arrows in the surface current distribution also indicates the magnitude. **(D)** Measured S_{11} curves of the stretchable wideband antenna under a tensile strain up to 15%. The two arrows indicate the two resonance states. **(E)** Measured and simulated bandwidth of the stretchable antenna with connected or unconnected parasitic arms and without parasitic arms.

dependent encapsulation, and the stiff PI layer underneath for strain isolation. As a result, the dual-resonance is well maintained in the fatigue testing. It should be noticed that the small conductivity variation from fabrication (~6%), temperature (~1.5%), or strain (~5.5%) has a negligible influence on S_{11} curves, indicating the

stable RF performance of the stretchable wideband antenna (Figure S18).

Because of the high dielectric constant and loss of human tissues, direct attachment of the stretchable wideband dipole antenna on the human wrist results in the disappearance of the "double-

Fig. 3. Characterization of the stretchable wideband antenna under large deformations or attached to human bodies. (A) Optical images of the stretchable wideband dipole antenna upon deformation (i.e., stretching, bending, and twisting). **(B)** Simulated strain distributions in the Ecoflex substrate and Ag/LIG layer of the stretchable wideband antenna upon bending and twisting deformations. **(C)** Measured S_{11} curves of the stretchable dipole antenna upon bending or twisting. **(D)** Simulated S_{11} curves of the stretchable wideband antenna attached above human wrists at various distances from 1 to 5 mm. When attached to human bodies, the "double-peak" characteristic of the stretchable dipole antenna disappears due to a high dielectric constant of human bodies. The double resonance gradually recovers at a distance of 4 mm. **(E)** Optical images of the stretchable wideband antenna placed on different parts of human bodies, including the arm, head, abdomen, or a nylon jacket, with **(F)** the corresponding measured S_{11} curves.

peak" characteristic in the measures and simulated S_{11} curve (Fig. 3EF). Placement of the antenna to the head leads to the smallest resonance shift, followed by the one on the arm and then the one on the abdomen, which is due to the different dielectric properties of human tissues. Despite the vanishing of the "double-peak" characteristic, the deformation-dependent resonance frequency can still be explored for wireless strain sensing (Movie S3).

However, the wideband and "double-peak" characteristic is gradually recovered as the distance between the antenna and human wrist increases to 5 mm (Fig. 3D). The recovery of dual-resonance characteristics is also verified by the observation of the inflection point in the imaginary part of impedance for a distance of 5 mm (Figure S28A). Also, the corresponding radiation pattern remains omnidirectional on the E-plane, which is close to that of a dipole

antenna in the free space (Figure S28B). Because of the reduced dielectric constant and loss in the surrounding environment introduced by the air gap, the resonant frequency also slightly shifts to a larger value from 2.20 to 2.30 GHz as the distance increased from 1 to 5 mm, which is smaller than the one without parasitic arms (from 1.91 to 2.25 GHz) (Figure S29). The results also indicate a relatively robust performance against the dielectric change of the environment or misposition. Inspired by these results, placing the antenna on a Nylon jacket (<3 mm thick) leads to a full recovery of the dual-resonance and wideband characteristics because of the air gap between the skin surface and jacket (Fig. 3D), demonstrating the potential in other forms of wearable devices. The use of the additional parasitic arm also helps reduce the specific absorption rate (SAR) by ~5% when the stretchable wideband dipole antenna is used in direct contact with or 5 mm away from human arms (Table S3 and Figure S30). Because dielectric constants and losses vary in different parts of the human body, the SAR value from stretchable wideband antennas and rectennas on different positions of the human body needs to be further evaluated.

Supplementary data related to this article can be found at https://doi.org/10.1016/j.mtphys.2021.100377.

1.4. Energy harvesting performance of stretchable wideband rectennas

Connecting the stretchable wideband dipole antenna with a rectifying circuit yields a stretchable rectenna (Fig. 4A). Configuring the Schottky diode SMS7630 (Skyworks Solutions Inc.) in a full-wave Greinacher rectifying circuit with a two-branch impedance matching circuit improves sensitivity and efficiency over a broad frequency range (1.75−2.45 GHz) [20]. By using a microwave oven as a convenient radiation source (Figure S31), the input power from the microwave oven radiation to the stretchable rectenna is programmed to decrease with the increasing distance (Fig. 4B). Though the Schottky diodes only require a low biasing voltage for a weak input signal, their RF-DC conversion efficiency is significantly reduced for μW operation to become around 0.1% [30], accounting for the decrease in the effective efficiency. Considering the additional loss in the antenna and matching circuit, it is indeed impressive to achieve an effective efficiency (see the Method section for calculation) of ~10% at a peak input power of 1 μW. This effective efficiency of 10% is significantly larger than the theoretical limit of the RF-DC conversion efficiency of 0.1% for the Schottky diode at a single frequency in μW operation, which is attributed to
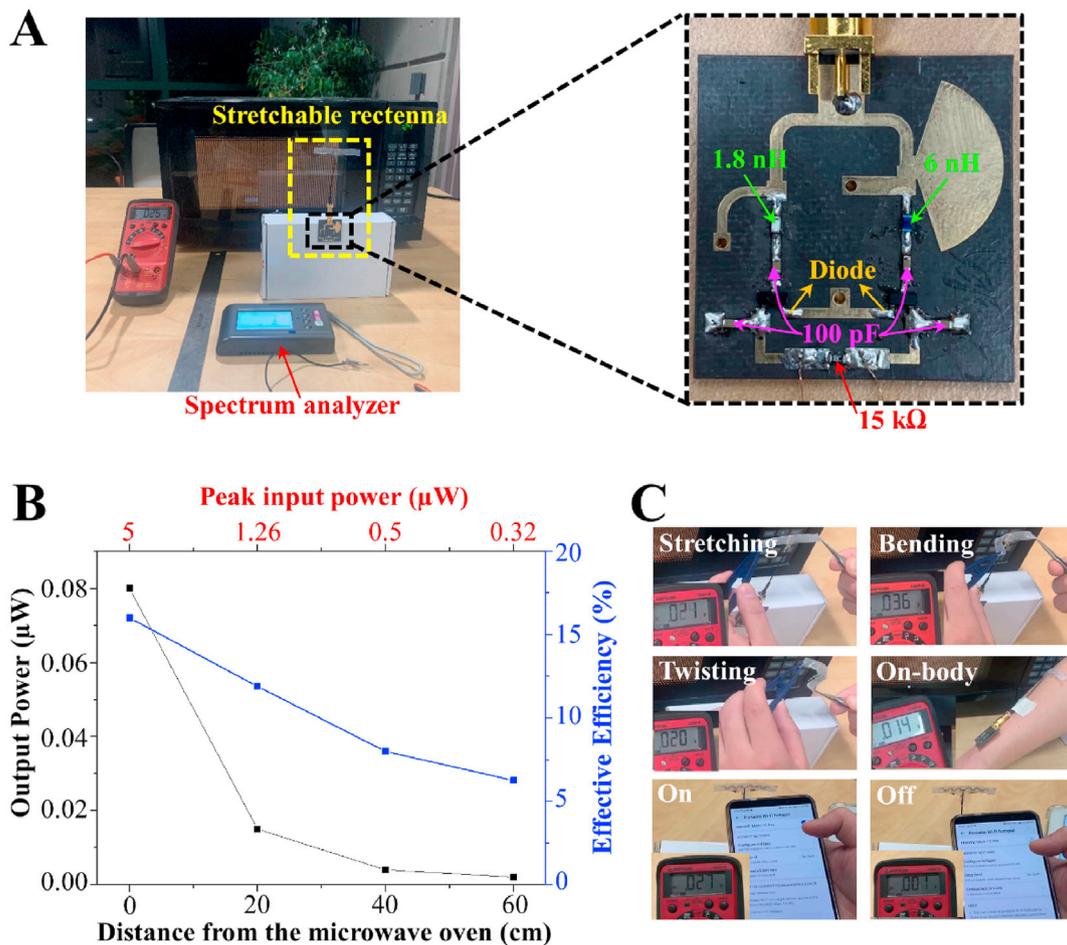
Fig. 4. Energy harvesting performance of the stretchable wideband rectenna. (A) Experimental setup to measure the energy harvesting performance of rectennas. A rectifier is designed to match 50 Ω input over the frequency from 2.0 to 2.5 GHz. A portable digital spectrum analyzer and a digital multimeter are used to measure the input RF power and the bias voltage over the resistance load. **(B)** Measured output power and effective efficiency as a function of the peak input power. **(C)** Optical images of the stretchable rectenna operated by the radiation of microwaves or cellphone hotspots under various deformations or on-body.

the stretchable wideband rectenna to combine received power over its wideband. The reported value is also significantly larger than that of the flexible rectenna reported in *Nature* [25]. The stretchable wideband rectenna is capable of harvesting the RF energy from cell phone hotspots (Movie S4), with a reliable and robust operation against various deformation modes such as stretching or twisting (Movie S5). The demonstrated stretchable wideband rectenna with high efficiency and mechanical compliance compares favorably over the previous reports (Table S4). Although the stretchable wideband rectenna has reduced on-body performance on the human arm (Fig. 4C), it still demonstrates its capability to harvest the ambient RF energy (Movie S6). Placing the antenna on a Nylon jacket rather than directly on human tissues can further boost the effective efficiency, approaching that in the free space (Movie S7). The energy harvesting efficiency of the stretchable wideband rectenna depends on the polarization alignment between the transmitter and the linearly polarized receiving dipole antenna. In addition to the use of a circularly polarized transmitter, the exploitation of dual-polarized dipole antennas or circularly polarized antennas can improve the output power efficiency for energy harvesting from the randomly polarized source.

Supplementary data related to this article can be found at https://doi.org/10.1016/j.mtphys.2021.100377.

For higher input powers, the conversion efficiency of the rectennas has been measured using the signal generator and anechoic chamber (Figure S32A). Similar calculations are performed except that the input power uses the integral power, other than the peak power. The differences between the simulation and experimental results are observed, especially at the higher received RF powers (Figure S32B). In addition to the fabrication error of the prototype, the difference may likely come from the SPICE model of the diode used in the ADS simulation, where the nonlinear response of commercial diodes cannot be accurately modeled. The previously reported results [25,43] also indicate the potential to prepare LIG-based flexible rectifying circuits to yield all-LIG flexible rectennas. Furthermore, the stretchable structures can be leveraged in the design of stretchable RF circuits [17,44] to result in fully stretchable rectennas. Similar to previously reported results, mechanically robust and stable electromagnetic properties of the stretchable wideband dipole antennas upon mechanical deformations can be easily applied to wireless communication for stretchable electronics in an integrated system [45]. Additionally, the design scheme reported here also offers stretchable rectennas with dual-band antennas for different application opportunities (Figure S33).

2. Conclusion

The concepts reported here combine the coupled mechanical-electromagnetic design approach with a simple laser-based fabrication to enable the stretchable wideband rectenna with high efficiency and compliant mechanical properties. Integrating this rectenna to harvest ambient RF energies with various low-power LIG sensors yields a new class of stretchable all-LIG electronics for future wearable electronics, implantable devices, and remote sensors. Because the antennas/rectennas with highly conductive radiation elements can lead to reduced power consumption, opportunities exist to explore more conductive materials (e.g., liquid metal or conventional metal with stretchable structures) in future works. To further reduce the absorption in the lossy tissues and improve the on-body energy harvesting performance, the metasurface ground [46,47] or stretchable patch antennas [17] with wideband designs [48,49] can be combined or exploited in the stretchable wideband rectenna. The methods for further improvement in the effective efficiency of the stretchable rectenna include the exploitations of the spin diode rectifiers to significantly enhance RF-DC conversion efficiency [50] or of stretchable wideband antennas with dual-polarization [24] (or circular-polarization [51]) to combine the randomly polarized electromagnetic field in the ambient environment.

3. Method

3.1. Fabrication of the stretchable wideband dipole antenna based on conductive laser-induced graphene (LIG) pattern with a metal surface coating

A soft, elastomeric substrate such as Ecoflex was first prepared by mixing the two components with a ratio of 1:1 on a ceramic plate coated with a layer of Ease Release (Mann Release Technologies, Inc.) to facilitate easy release of the substrate. By using a doctor blade, the substrate thickness was controlled to be ca. 1 mm. After rinsing with ethanol and distilled (DI) water, the polyimide (PI) film was coated with the 2% APTES (diluted in ethanol) by dipping in the solution for 1 min, followed by rinsing with DI water. Upon completion of drying, both the PI film and Ecoflex substrate were treated with UV/Ozone for 2 min to remove organic contaminants for improved surface bonding [52]. Next, a CO_2 laser (Universal M – 360) was used to transform the PI film into LIG patterns designed with AutoCAD. After aligning the PI film onto the Ecoflex substrate, the raster mode (power of 16% and speed of 10%) and the vector mode (with a 10% power and 3% speed) were selected to create and carve the desired LIG patterns, respectively. Pulses per inch (PPI) of 1000 and a high image density were adopted during the engraving and cutting processes. Before peeling off the excessive PI film from carving (i.e., the region outside the outlines of the LIG patterns, self-mask), silver nanoparticle (AgNP) ink (JS-A911, Novacentix Inc.) was sprayed and kept at room temperature for 20 s to vaporize the solvent in ink. Peeling off the PI self-mask left the AgNP ink only on the LIG patterns. Upon exposure of a xenon light (Xenon Corporation, X-1100) with three pulses (i.e., single pulse mode with a duration of 529 μs at an energy of 1000 J and a voltage of 3000 V), a conductive Ag pathway formed on the LIG pattern because of the xenon-induced sintering of the AgNPs from transient high temperature. Lastly, annealing the sample at 80 °C for 3 h led to strong covalent bonding between the Ag/LIG pattern and the Ecoflex substrate. The remaining PI layer underneath the Ag/LIG pattern naturally served as a stiffener to help reduce the local strain in the conductive pattern upon mechanical deformations (e.g., stretching, bending, or twisting) because of strain isolation [53,54]. After connecting the stretchable antennas to the feed line by coaxial cables for easy hand soldering, another thin layer (50 μm) of a soft, elastomeric polymer was used to encapsulate the antennas. The encapsulation layer was designed with spatial-dependent modulus, which used a soft Ecoflex layer in the region of dipole arms and a stiff PDMS (Sylgard 184) layer with a 1:4 mixing ratio in the region of soldering locations for enhanced stretchability [14].

Characterizations and measurements of temperature/humidity sensors and electrodes:

The temperature sensor was first placed on a hotplate with accurate temperature control for calibration. Its resistances at different temperatures were measured by a sourcemeter (Keithley 2401). The relative resistance changes versus temperature provided the calibration curve for the temperature sensor. The humidity sensor was calibrated by placing it in a container with various controlled relative humidity levels set by different saturated salt solutions. As confirmed by a commercial humidity gauge (AcuRite 00613 MB), the saturated salt solutions of NaOH, $Na_2Cr_2O_7$, NaCl, KCl, and Na_2HPO_4 corresponded to a relative humidity level of 22%, 54%, 75%, 85%, and 90%, respectively. The impedance and

capacitance of the humidity sensor in the environment with different relative humidity levels were measured by an LCR meter (Keysight E4980A/AL Precision LCR meter). The sensing performance of the sensors under deformations was measured by the same experimental setup after they were stretched to a tensile strain of 20% and then clamped onto glass slides. As for the measurements of electrophysiological (EP) signals (e.g., electrocardiogram, ECG), two LIG electrodes (3 mm × 3 mm) were first attached to the chest of a human subject. Connection of the electrodes to the data acquisition system (Powerlab 16/35, ADInstruments) provided real-time ECG measurements."

3.2. Characterization of stretchable dipole antennas

The dielectric properties of silicone polymers such as Ecoflex and PDMS used for the substrate and encapsulation layer were first measured by a resonant mode dielectrometer (RMD-C-100, GDK Product Inc.) Mechanical stretching test on Ecoflex, PDMS, PI, LIG/PI, and Ag/LIG/PI with a rectangular shape was carried out with the Dynamic Mechanical Analysis (DMA) (TA Instruments, Q800). The electrical resistance of the LIG and Ag/LIG composite was measured by a SourceMeter (Keithley 2401) to yield their sheet resistance/conductivity. The electromechanics properties of Ag/LIG/PI with straight or serpentine patterns under stretching was also measured. Raman spectrum of the LIG was obtained by Horiba (HORIBA, Ltd.). The morphologies of the LIG pattern and Ag/LIG composites were characterized by NanoSEM630 (FEI Company). The tensile strain in the range from 0% to 15% was applied to the stretchable dipole antennas by a custom-built stretcher. The radiation properties of the stretched antennas were characterized by a network analyzer (Keysight E5071C).

3.3. Mechanics simulation

The finite element analysis was carried out by a commercial software ABAQUS (ABAQUS 6.14, ABAQUS Inc.) to yield the deformed configuration and strain distribution of dipole antennas upon a given tensile strain. LIG (or Ag/LIG) was treated with a skin layer on the surface of the elastomeric substrate in order to reduce the computation load. The soft substrate and LIG (or Ag/LIG) were modeled by eight-node 3D solid elements (C3D8R) and four-node shell elements (S4R), respectively. Mesh sizes were refined to ensure convergence for computational accuracy. Both buckling and non-buckling were considered in the analysis. The Young's moduli and Poisson's ratios are $E_{Ag/LIG} = 0.93$ GPa (from measurements) and $\nu_{Ag/LIG} = 0.365$ for the Ag/LIG; and $E_{sub} = 0.05$ MPa (from measurements) and $\nu_{sub} = 0.49$ for the Ecoflex substrate; and $E_{PDMS} = 1.4$ MPa (from measurements) and $\nu_{PDMS} = 0.49$ [55] for the Ecoflex substrate.

3.4. Electromagnetic simulation

The reflection coefficient (S_{11}) and impedance of stretchable antennas were calculated by the finite element method with a commercial software ANSYS high-frequency electromagnetic field simulation (HFSS) package in the electromagnetic simulation. After importing the deformed configurations obtained from the mechanical simulations into ANSYS HFSS, tetrahedron elements with adaptive meshing convergence were adopted. The convergence criterion (S-maximal delta S) is set to 0.02 with up to 15 passes. The Ag/LIG composite layers in stretchable antennas were modeled by a finite conductivity boundary with prescribed thicknesses. Because of the negligible influence on the electromagnetic simulation, the PI layer beneath the conductive Ag/LIG pattern was not included in the simulation model for the sake of efficiency. Similarly, antennas

were imported into a model with human bodies in CST software to simulate the specific absorption rate (SAR). Antennas were placed on the top of wrists at various distances (from 0 to 5 mm).

3.5. Design and fabrication of the rectifier

The rectifier was designed with the Advanced Design System (ADS, Keithley Instrument Company). Following the standard etching process of the Duroid 5880 board (thickness of 1.57 mm and dielectric constant of 2.2), the capacitors (Yageo), inductors (Johanson Technology Inc.), resistors (Yageo), and Schottky diode (SMS7630, Skyworks Solutions Inc.) purchased from Digikey Electronics were manually soldered on the board to complete the fabrication of the rectifier.

3.6. Characterization of the stretchable wideband rectenna

Microwave ovens and cell phone hotspots were used as electromagnetic energy sources. A portal spectrum analyzer (EMF-390, GQ Electronics LLC) was used to measure the radiation power at different distances from the electromagnetic energy sources. The corresponding output power from the proposed rectenna was calculated from the voltage across the resistance load R_L measured by a digital multimeter. The effective efficiency was then obtained from $V_{DC}^2/(R_L \times P_r)$, where V_{DC} is the measured output voltage and P_r is the input peak power from the portal spectrum analyzer. The energy harvesting performance of the proposed rectenna under deformations was verified by manual bending or twisting. On-body measurement was carried out by attaching the stretch wideband dipole antenna on human arms and fixing the rectifier circuit with medical tapes. The conversion efficiency at higher input power was measured using the signal generator and anechoic chamber. The frequency-adjustable signals generated by an RF signal generator (Keysight 83623L) were amplified by a 30-dB gain power amplifier (PA) and transmitted by a calibrated horn antenna R&SHF906. The amplified RF power was shunted by a Nadar 20 dB directional coupler where one way of the coupler fed the transmitting horn, while another way fed the power meter of Agilent E4416A to measure the transmitting power. The rectenna was placed at a distance L of 1 m from the transmitting horn. A multimeter measured the output voltage across the load of the rectenna. The transmitting power (P_t) of the horn antenna was measured by a power meter in dBm. At the wavelength of interest ($\lambda = c/f$) with c being the speed of light, the received power (P_r) by the rectenna was calculated by the Friis equation

$$P_r = P_t + G_t + G_r + 20\log_{10}\frac{\lambda}{4\pi L}, \tag{1}$$

where G_t is the realized gain of the horn in dBi and G_r is the realized gain of the stretchable rectenna in dBi.

Appendix A. Supplementary data

Supplementary data to this article can be found online at https://doi.org/10.1016/j.mtphys.2021.100377.

Credit author statement

Jia Zhu: Data curation, Formal analysis, Investigation, Zhihui Hu: Materials synthesis; Data curation, Chaoyun Song: Measurement; Data curation; Investigation; Writing-review, Ning Yi: Data curation, Zhaozheng Yu: Measurement, Zhendong Liu: Materials synthesis, Shangbin Liu: Materials synthesis, Mengjun Wang: Investigation, Michael Gregory Dexheimer: Measurement, Jian Yang: Investigation; Writing-review, Huanyu Cheng: Resources; Supervision; Project administration; Writing-review.

References

[1] Y. Yang, W. Gao, Chem. Soc. Rev. 48 (2019) 1465−1491.
[2] X. Wang, Z. Liu, T. Zhang, Small 13 (2017) 1602790.
[3] Q. Shi, T. He, C. Lee, Nanomater. Energy 57 (2019) 851−871.
[4] A.D. Mickle, S.M. Won, K.N. Noh, J. Yoon, K.W. Meacham, Y. Xue, L.A. McIlvried, B.A. Copits, V.K. Samineni, K.E. Crawford, D.H. Kim, P. Srivastava, B.H. Kim, S. Min, Y. Shiuan, Y. Yun, M.A. Payne, J. Zhang, H. Jang, Y. Li, H.H. Lai, Y. Huang, S.I. Park, R.W.t. Gereau, J.A. Rogers, Nature 565 (2019) 361−365.
[5] J. Kim, A. Banks, Z. Xie, S.Y. Heo, P. Gutruf, J.W. Lee, S. Xu, K.I. Jang, F. Liu, G. Brown, J. Choi, J.H. Kim, X. Feng, Y. Huang, U. Paik, J.A. Rogers, Adv. Funct. Mater. 25 (2015) 4761−4767.
[6] J. Kim, M. Kim, M.-S. Lee, K. Kim, S. Ji, Y.-T. Kim, J. Park, K. Na, K.-H. Bae, H. Kyun Kim, F. Bien, C. Young Lee, J.-U. Park, Nat. Commun. 8 (2017) 14997.
[7] H. Araki, J. Kim, S. Zhang, A. Banks, K.E. Crawford, X. Sheng, P. Gutruf, Y. Shi, R.M. Pielak, J.A. Rogers, Adv. Funct. Mater. 27 (2017) 1604465.
[8] J. Kim, P. Gutruf, A.M. Chiarelli, S.Y. Heo, K. Cho, Z. Xie, A. Banks, S. Han, K.I. Jang, J.W. Lee, K.T. Lee, X. Feng, Y. Huang, M. Fabiani, G. Gratton, U. Paik, J.A. Rogers, Adv. Funct. Mater. 27 (2017) 1604373.
[9] X. Cao, M. Zhang, J. Huang, T. Jiang, J. Zou, N. Wang, Z.L. Wang, Adv. Mater. 30 (2018) 1704077.
[10] Y. Jie, J. Ma, Y. Chen, X. Cao, N. Wang, Z.L. Wang, Adv. Energy Mater. 8 (2018) 1802084.
[11] Y. Chen, Y. Cheng, Y. Jie, X. Cao, N. Wang, Z.L. Wang, Energy Environ. Sci. 12 (2019) 2678−2684.
[12] J.A. Hagerty, F.B. Helmbrecht, W.H. McCalpin, R. Zane, Z.B. Popovic, IEEE Trans. Microw. Theor. Tech. 52 (2004) 1014−1024.
[13] A. Bakytbekov, T.Q. Nguyen, C. Huynh, K.N. Salama, A. Shamim, Nanomater. Energy 53 (2018) 587−595.
[14] M. Kubo, X. Li, C. Kim, M. Hashimoto, B.J. Wiley, D. Ham, G.M. Whitesides, Adv. Mater. 22 (2010) 2749−2752.
[15] J.-H. So, J. Thelen, A. Qusba, G.J. Hayes, G. Lazzi, M.D. Dickey, Adv. Funct. Mater. 19 (2009) 3632−3637.
[16] Z. Chen, J. Xi, W. Huang, M.M.F. Yuen, Sci. Rep. 7 (2017) 10958.
[17] J. Zhu, J.J. Fox, N. Yi, H. Cheng, ACS Appl. Mater. Interfaces 11 (2019) 8867−8877.
[18] T. Chang, Y. Tanabe, C.C. Wojcik, A.C. Barksdale, S. Doshay, Z. Dong, H. Liu, M. Zhang, Y. Chen, Y. Su, T.H. Lee, J.S. Ho, J.A. Fan 27 (2017) 1703059.
[19] Y.-S. Kim, A. Basir, R. Herbert, J. Kim, H. Yoo, W.-H. Yeo, ACS Appl. Mater.

[20] C. Song, Y. Huang, J. Zhou, J. Zhang, S. Yuan, P. Carter, IEEE Trans. Antenn. Propag. 63 (2015) 3486−3495.
[21] A. Arriola, J.I. Sancho, S. Brebels, M. Gonzalez, W.D. Raedt, IET Microwaves, Antennas & Propagation, Institution of Engineering and Technology, 2011, pp. 852−859.
[22] J.-M. Floc H, A. El Sayed Ahmad, Int. J. Electromagn. Appl. 2 (2012) 120−128.
[23] H.H. Tran, I. Park, T.K. Nguyen, IEEE Antenn. Wireless Propag. Lett. (2017), 1-1.
[24] C. Song, Y. Huang, J. Zhou, P. Carter, S. Yuan, Q. Xu, Z. Fei, IEEE Trans. Ind. Electron. 64 (2017) 3950−3961.
[25] X. Zhang, J. Grajal, J.L. Vazquez-Roy, U. Radhakrishna, X. Wang, W. Chern, L. Zhou, Y. Lin, P.−C. Shen, X. Ji, X. Ling, A. Zubair, Y. Zhang, H. Wang, M. Dubey, J. Kong, M. Dresselhaus, T. Palacios, Nature 566 (2019) 368−372.
[26] W. Zeng, L. Shu, Q. Li, S. Chen, F. Wang, X.M.J.A.m. Tao, 26 (2014) 5310-5336.
[27] T.R. Ray, J. Choi, A.J. Bandodkar, S. Krishnan, P. Gutruf, L. Tian, R. Ghaffari, J.A.J.C.r. Rogers 119 (2019) 5461−5533.
[28] A. Dewan, S.U. Ay, M.N. Karim, H.J.J.o.P. S, Beyenal 245 (2014) 129−143.
[29] T.-W. Yoo, K. Chang, Techniques 40 (1992) 1259−1266.
[30] B. Fang, M. Carpentieri, S. Louis, V. Tiberkevich, A. Slavin, I.N. Krivorotov, R. Tomasello, A. Giordano, H. Jiang, J. Cai, Phys. Rev. Appl. 11 (2019): 014022.
[31] S. Hemour, Y. Zhao, C.H.P. Lorenz, D. Houssameddine, Y. Gui, C.-M. Hu, K. Wu, Techniques 62 (2014) 965−976.
[32] K. Agarwal, Y. Guo, Asia-Pacific Symposium on Electromagnetic Compatibility (APEMC)2015, 2015, pp. 154−157.
[33] B.J. DeLong, A. Kiourti, J.L. Volakis, IEEE J. Electromagnet., RF Microwaves Med. Biol. 2 (2018) 64−69.
[34] M.K. Hosain, A.Z. Kouzani, M.F. Samad, S.J. Tye, IEEE Access 3 (2015) 223−234.
[35] Y. Gao, Y. Zhang, X. Wang, K. Sim, J. Liu, J. Chen, X. Feng, H. Xu, C. Yu, Sci. Adv. 3 (2017): e1701222.
[36] J.M.J.A.M R. Ye, D.K. James, Tour 31 (2019) 1803621.
[37] B. Sun, R.N. McCay, S. Goswami, Y. Xu, C. Zhang, Y. Ling, J. Lin, Z. Yan, Adv. Mater. 30 (2018) 1804327.
[38] H.U. Chung, B.H. Kim, J.Y. Lee, J. Lee, Z. Xie, E.M. Ibler, K. Lee, A. Banks, J.Y. Jeong, J. Kim, C. Ogle, D. Grande, Y. Yu, H. Jang, P. Assem, D. Ryu, J.W. Kwak, M. Namkoong, J.B. Park, Y. Lee, D.H. Kim, A. Ryu, J. Jeong, K. You, B. Ji, Z. Liu, Q. Huo, X. Feng, Y. Deng, Y. Xu, K.-I. Jang, J. Kim, Y. Zhang, R. Ghaffari, C.M. Rand, M. Schau, A. Hamvas, D.E. Weese-Mayer, Y. Huang, S.M. Lee, C.H. Lee, N.R. Shanbhag, A.S. Paller, S. Xu, J.A. Rogers, Science 363 (2019): eaau0780.
[39] X. Huang, Y. Liu, H. Cheng, W.-J. Shin, J.A. Fan, Z. Liu, C.-J. Lu, G.-W. Kong, K. Chen, D. Patnaik, S.-H. Lee, S. Hage-Ali, Y. Huang, J.A. Rogers, Adv. Funct. Mater. 24 (2014) 3846−3854.
[40] Y. Zhao, S. Gao, J. Zhu, J. Li, H. Xu, K. Xu, H. Cheng, X. Huang, ACS Omega 4 (2019) 9522−9530.
[41] L. Yang, N. Yi, J. Zhu, Z. Cheng, X. Yin, X. Zhang, H. Zhu, H. Cheng, J. Mater. Chem. 8 (2020) 6487−6500.
[42] N. Yi, Z. Cheng, H. Li, L. Yang, J. Zhu, X. Zheng, Y. Chen, Z. Liu, H. Zhu, H. Cheng, Mater. Today Phys. 15 (2020) 100265.
[43] B.T. Malik, V. Doychinov, S.A.R. Zaidi, I.D. Robertson, N. Somjit, R. Richardson, N. Chudpooti, Research, Invention, and Innovation Congress (RI2C)2019, 2019, pp. 1−5.
[44] T. Chang, Y. Tanabe, C.C. Wojcik, A.C. Barksdale, S. Doshay, Z. Dong, H. Liu, M. Zhang, Y. Chen, Y. Su, T.H. Lee, J.S. Ho, J.A. Fan, Adv. Funct. Mater. 27 (2017) 1703059.
[45] A.M. Hussain, F.A. Ghaffar, S.I. Park, J.A. Rogers, A. Shamim, M.M. Hussain, Adv. Funct. Mater. 25 (2015) 6565−6575.
[46] M. El Badawe, T.S. Almoneef, O.M. Ramahi, AIP Adv. 7 (2017): 035112.
[47] S.B. Glybovski, S.A. Tretyakov, P.A. Belov, Y.S. Kivshar, C.R.J.P.r. Simovski, 634 (2016) 1-72.
[48] W.P. K.Y. Lam, K.-M. Luk, K.F. Lee, H. Wong, K.B.J.I.A. Ng Letters 10 (2011) 87−90.
[49] W. He, R. Jin, J. Geng, Propagation 56 (2008) 893−895.
[50] O. Prokopenko, I. Krivorotov, E. Bankowski, T. Meitzler, S. Jaroch, V. Tiberkevich, A.J.J.o.A.P. Slavin 111 (2012) 123904.
[51] W. Lin, H. Wong, Propagation 63 (2015) 5938−5944.
[52] Z. Yan, F. Zhang, F. Liu, M. Han, D. Ou, Y. Liu, Q. Lin, X. Guo, H. Fu, Z. Xie, M. Gao, Y. Huang, J. Kim, Y. Qiu, K. Nan, J. Kim, P. Gutruf, H. Luo, A. Zhao, K.-C. Hwang, Y. Huang, Y. Zhang, J.A. Rogers, Sci. Adv. 2 (2016): e1601014.
[53] Y. Liu, Z. Liu, B. Zhu, J. Yu, K. He, W.R. Leow, M. Wang, B.K. Chandran, D. Qi, H. Wang, G. Chen, C. Xu, X. Chen, Adv. Mater. 29 (2017) 1701780.
[54] A. Romeo, Q. Liu, Z. Suo, S.P. Lacour, Appl. Phys. Lett. 102 (2013) 131904.
[55] I.D. Johnston, D.K. McCluskey, C.K.L. Tan, M.C. Tracey, J. Micromech. Microeng. 24 (2014): 035017.